Supplementary Material for "Hyper-Laplacian Regularized Unidirectional Low-rank Tensor Recovery for Multispectral Image Denoising"

1. Solution to Problem (6) in Main Text

The original problem is shown as follow:

$$\hat{\boldsymbol{\mathcal{X}}} = \arg\min_{\boldsymbol{\mathcal{X}}} \frac{1}{2}||\boldsymbol{\mathcal{X}} - \boldsymbol{\mathcal{Y}}||_F^2 + \frac{\alpha}{2}||\boldsymbol{\mathcal{D}} - \nabla_z \boldsymbol{\mathcal{X}} - \frac{\boldsymbol{\mathcal{J}}}{\alpha}||_F^2 + \omega \sum\nolimits_i \frac{1}{\lambda_i^2}||\mathcal{R}_i \boldsymbol{\mathcal{X}} - \boldsymbol{\mathcal{L}}_i||_F^2. \tag{1}$$

The main difficulty for the Fourier transform in (1) lies in the fact that $\boldsymbol{\mathcal{X}}$ is involved with the cubic operation $\mathcal{R}_i$. Thus, it is natural for us to split the $\boldsymbol{\mathcal{X}}$ in the third term from other terms. We introduce another auxiliary variable $\boldsymbol{\mathcal{Z}}$, by applying ADMM to (1), we obtain

$$\left\{\hat{\boldsymbol{\mathcal{X}}}, \hat{\boldsymbol{\mathcal{Z}}}\right\} = \arg\min_{\boldsymbol{\mathcal{X}},\boldsymbol{\mathcal{Z}}} \frac{1}{2}||\boldsymbol{\mathcal{X}} - \boldsymbol{\mathcal{Y}}||_F^2 + \frac{\alpha}{2}||\boldsymbol{\mathcal{D}} - \nabla_z \boldsymbol{\mathcal{X}} - \frac{\boldsymbol{\mathcal{J}}}{\alpha}||_F^2 + \omega \sum\nolimits_i \frac{1}{\lambda_i^2}||\mathcal{R}_i \boldsymbol{\mathcal{Z}} - \boldsymbol{\mathcal{L}}_i||_F^2 + \frac{\beta}{2}||\boldsymbol{\mathcal{Z}} - \boldsymbol{\mathcal{X}} - \frac{\boldsymbol{\mathcal{J}}_1}{\beta}||_F^2, \tag{2}$$

where $\boldsymbol{\mathcal{Z}} \in \mathbb{R}^{M\times N\times B}$ is an auxiliary variable, $\boldsymbol{\mathcal{J}}_1$ is the Lagrangian multiplier, β and is a positive scalar. The optimization of (2) consists of the following iterations:

$$\begin{aligned}
&\boldsymbol{\mathcal{X}}^{(l+1)} = \arg\min_{\boldsymbol{\mathcal{X}}} \frac{1}{2}||\boldsymbol{\mathcal{X}} - \boldsymbol{\mathcal{Y}}||_F^2 + \frac{\alpha}{2}||\boldsymbol{\mathcal{D}} - \nabla_z \boldsymbol{\mathcal{X}} - \frac{\boldsymbol{\mathcal{J}}}{\alpha}||_F^2 + \frac{\beta}{2}||\boldsymbol{\mathcal{Z}}^{(l)} - \boldsymbol{\mathcal{X}} - \frac{\boldsymbol{\mathcal{J}}_1^{(l)}}{\beta}||_F^2,\\
&\boldsymbol{\mathcal{Z}}^{(l+1)} = \arg\min_{\boldsymbol{\mathcal{Z}}} \omega \sum\nolimits_i \frac{1}{\lambda_i^2}||\mathcal{R}_i \boldsymbol{\mathcal{Z}} - \boldsymbol{\mathcal{L}}_i||_F^2 + \frac{\beta}{2}||\boldsymbol{\mathcal{Z}} - \boldsymbol{\mathcal{X}}^{(l+1)} - \frac{\boldsymbol{\mathcal{J}}_1}{\beta}||_F^2,\\
&\boldsymbol{\mathcal{J}}_1^{(l+1)} = \boldsymbol{\mathcal{J}}_1^{(l+1)} + \beta^{(l)}(\boldsymbol{\mathcal{X}}^{(l+1)} - \boldsymbol{\mathcal{Z}}^{(l+1)})\\
&\beta^{(l+1)} = \rho\beta^{(l+1)},
\end{aligned} \tag{3}$$

where $\rho > 1$ is a constant. Thus the variables $\boldsymbol{\mathcal{X}}$ and $\boldsymbol{\mathcal{Z}}$ can be solved with closed-form solution efficiently:

$$\boldsymbol{\mathcal{X}}^{(l+1)} = \boldsymbol{\mathcal{F}}^{-1}\left(\frac{\boldsymbol{\mathcal{F}}\left(\boldsymbol{\mathcal{Y}} + \nabla_z^T(\alpha^{(l)}\boldsymbol{\mathcal{D}} - \boldsymbol{\mathcal{J}}) + (\beta^{(l)}\boldsymbol{\mathcal{Z}}^{(l)} - \boldsymbol{\mathcal{J}}_1^{(l)})\right)}{1 + \alpha^{(l)}(\boldsymbol{\mathcal{F}}(\nabla_z))^2 + \beta^{(l)}}\right) \tag{4}$$

$$\boldsymbol{\mathcal{Z}}^{(l+1)} = \left(2\lambda_i^2 \sum\nolimits_i \mathcal{R}_i^T \mathcal{R}_i + \beta^{(l)}\boldsymbol{\mathcal{I}}\right)^{-1} \times \left(2\lambda_i^2 \sum\nolimits_i \mathcal{R}_i^T \boldsymbol{\mathcal{L}}_i + \beta^{(l)}\boldsymbol{\mathcal{X}}^{(l+1)} + \boldsymbol{\mathcal{J}}_1^{(l)}\right) \tag{5}$$

where $\boldsymbol{\mathcal{F}}(\bullet)$ denotes the *n*-D fast Fourier transform and $\boldsymbol{\mathcal{F}}^{-1}(\bullet)$ the inverse transform, $\boldsymbol{\mathcal{I}}$ is the identity tensor, $\mathcal{R}_i^T\mathcal{R}_i$ means the number of overlapping cubics that cover the pixel location, and $\mathcal{R}_i^T\boldsymbol{\mathcal{L}}_i$ means the sum value of all overlapping reconstruction cubics that cover the pixel location. Thus, Eq. (4) can be computed in Fourier domain and Eq. (5) can be computed in pixel-to-pixel level division with tensor format. In fact, the two auxiliary variables $\boldsymbol{\mathcal{D}}$ in main text and $\boldsymbol{\mathcal{Z}}$ in this supplementary can be introduced at the same time, without any sequence. Due to the page limitation, we place the solution of $\boldsymbol{\mathcal{Z}}$ in the supplementary.

2. Extension to LLRT-RPCA

As the reviewers concerned, the real noises in HSI are always complex with more than random noise. Indeed, the stripe line noise is another issue, which usually coexists with the random noise. To some degree, once the stripe arises in the HSI,

Algorithm 1 The hyper-Laplacian regularized unidirectional low-rank tensor (LLRT) algorithm

Require: Input image $\boldsymbol{\mathcal{Y}}$

Initialize:
• Set parameters μ, α, ω and the noise level;
• Set $\boldsymbol{J}^{(1)} = 0, \boldsymbol{J}_1^{(1)} = 0$;
• Similar cubics grouping for each target cubic to form the 3-order tensor;
for n=1:N **do**
  obtain $\boldsymbol{\mathcal{L}}_i$ by solving Eq. (3)(main manuscript);
  for (Solving Eq. (4)(main manuscript)) l=1:L **do**
    Solve Eq. (5) for $\boldsymbol{\mathcal{D}}^{(l+1)}$(main manuscript);
    Solve Eq. (3) for $\boldsymbol{\mathcal{X}}^{(l+1)}$ and $\boldsymbol{\mathcal{Z}}^{(l+1)}$(Supplementary);
  end for
  If mod(n, T)=0, update cubic grouping;
  Output the clear image $\boldsymbol{\mathcal{X}}$ if $n = N$.
end for

Ensure: Clean Image $\boldsymbol{\mathcal{X}}$.

it is more urgent to remove them than the random noise. In recent years, the stripe noise removal has received more and more attention. For [5, 1, 3], this kind of methods hold the point that the stripe line is an structure noise, and introduce the mixture of Gaussians (MoG) noise assumption also its variants to adapt the real noise characteristics of natural HSI, so as to accommodate various noise shapes encountered in real applications. Another research direction starts from the image decomposition perspective [7, 4, 2], in which the stripe noise is regarded as an structural line pattern component, equally treated with the image component. Our LLRT-RPCA method follows the image decomposition manner. Thus, the problem can be transferred to how to construct two reasonable measurements to differ the image component from the stripe component. In the main paper, we have given the detailed analysis about the key prior for the MSI image component modeling. And the focus of this paper is to address the image modeling issue. As for the stripe component modeling, it is out the scope of this work. The relevant work has been submitted recently. Interested readers may keep an eye on our future work. Here we just introduce the common used L_1 norm for the stripe component, just as the classical RPCA [6] regularizing the gross error:

$$\left\{\hat{\boldsymbol{\mathcal{X}}}, \hat{\boldsymbol{\mathcal{L}}}_i, \hat{\boldsymbol{\mathcal{E}}}\right\} = \arg\min_{\boldsymbol{\mathcal{X}}, \boldsymbol{\mathcal{L}}_i, \boldsymbol{\mathcal{E}}} \frac{1}{2}||\boldsymbol{\mathcal{X}} + \boldsymbol{\mathcal{E}} - \boldsymbol{\mathcal{Y}}||_F^2 + \mu||\nabla_z \boldsymbol{\mathcal{X}}||_p + \omega \sum\nolimits_i \left(\frac{1}{\lambda_i^2}||\mathcal{R}_i \boldsymbol{\mathcal{X}} - \boldsymbol{\mathcal{L}}_i||_F^2 + rank_2(\boldsymbol{\mathcal{L}}_i)\right) + \tau||\boldsymbol{\mathcal{E}}||_1, \quad (6)$$

where $\boldsymbol{\mathcal{E}}$ represents the gross error namely the stripe noise, and τ is the regularization parameter. The optimization is similar to that of LLRT, with additional step for the gross error $\boldsymbol{\mathcal{E}}$.

3. More results

In this document, we present more noise removal results, which are not included in the main paper due to page limit.

3.1. Simulated Experimental Results

Figure 1 to Figure 5 present five visual comparison results of various methods on simulated hyperspectral and color images under different noise levels. From the visual results, we can observe that the proposed LLRT method consistently obtains the best performance in terms of both finer-grained textures and coarser-grained structures for different multispectral images. For the quantitative results, LLRT outperforms the second best results ISTReg by a large marginal. In Fig. 6, we plot the PSNR values of each band of one single image *cloth*. In Fig. 7, we plot the average PSNR values of all bands of each image. For each band and each image, our method consistently obtains the best result.

3.2. Real Experimental Results

Figure 8 and Figure 9 present two visual comparison results of various methods on real hyperspectral and color image, respectively. It can be observed that the images restored by our method are more visually pleasant with more detailed information and less color distortion artifact. Further, we test the LLRT-RPCA method on the mixed noisy HSI dataset *Urban*, and the results are shown in Fig. 10.

3.3. The Analysis of Tensor Low-rank Prior Along Each Mode

The non-local patch number dimension is more evidently low-rank (here we give another example image *clay* as shown in Fig. 11), and neglecting others can help improve efficiency. However, it might be not so rational that neglecting other useful low-rankness along other dimensions, especially in spectrum, can help improve MSI recovery quality. In our paper, we capture the most low-rank subspace along the non-local mode. Here, we give a detailed comparison of the combination of low-rank prior along each mode, as shown in Fig. 12. Here, we have following observations.

- For single mode-based low-rank prior (red, purple, green curve), we can find that the non-local self-similarity mode achieved the best performance, which further validates the conclusion in the main paper: ***the structure correlation along the non-local self-similarity mode is much stronger than that of the spatial or spectral mode***.
- The spatial mode low-rank always bring negative influence to the final performance (compare purple and cyan, also grey and blue), since we have stated in the main paper that their low-rank assumptions cannot be met.
- The spectral mode low-rank does facilitate the final recovery result (compare purple and grey). That is to say the spectral correlation spectral correlation property can facilitate the MSI recovery results.
- In this work, we introduce the patch-free hyper-Laplacian prior to model the spectral correlation. The grey (nonlocal + spectral low-rank) and yellow (proposed hyper-Laplacian regularized nonlocal low-rank) curves have achieved the best two performances. However, the processing time of the proposed method is much less than that of the grey curve, since the additional SVD operation occupied much of the processing time.

From the above analysis, we can conclude that the non-local self-similarity is the key property contributing to MSI denoising performance, and the spectral correlation property does facilitate the final recovery result. Our focus is not about the specific priors but why and how we use them in reasonable manner for MSI modeling. Here, we choose the hyper-Laplacian to model the spectral correlation not the low-rank, is for one hand to reduce the processing time, and for the other hand to suppress the visual ringing artifact.

References

[1] X. Cao, Y. Chen, Q. Zhao, D. Meng, Y. Wang, D. Wang, and Z. Xu. Low-rank matrix factorization under general mixture noise distributions. In *ICCV*, pages 1493–1501, 2015. 2

[2] Y. Chang, L. Yan, T. Wu, and S. Zhong. Remote sensing image stripe noise removal: From image decomposition perspective. *IEEE TGRS*, 54(12):7018–7031, 2016. 2

[3] Y. Chen, X. Cao, Q. Zhao, D. Meng, and Z. Xu. Denoising hyperspectral image with non-iid noise structure. *arXiv:1702.00098*, 2017. 2

[4] W. He, H. Zhang, L. Zhang, and H. Shen. Total-variation-regularized low-rank matrix factorization for hyperspectral image restoration. *IEEE TGRS*, 54(1):178–188, 2016. 2

[5] D. Meng and F. D. L. Torre. Robust matrix factorization with unknown noise. In *ICCV*, pages 1337–1344, 2013. 2

[6] J. Wright, A. Ganesh, S. Rao, Y. Peng, and Y. Ma. Robust principal component analysis: Exact recovery of corrupted low-rank matrices via convex optimization. In *NIPS*, pages 2080–2088, 2009. 2

[7] H. Zhang, W. He, L. Zhang, H. Shen, and Q. Yuan. Hyperspectral image restoration using low-rank matrix recovery. *IEEE TGRS*, 52(8):4729–4743, 2014. 2

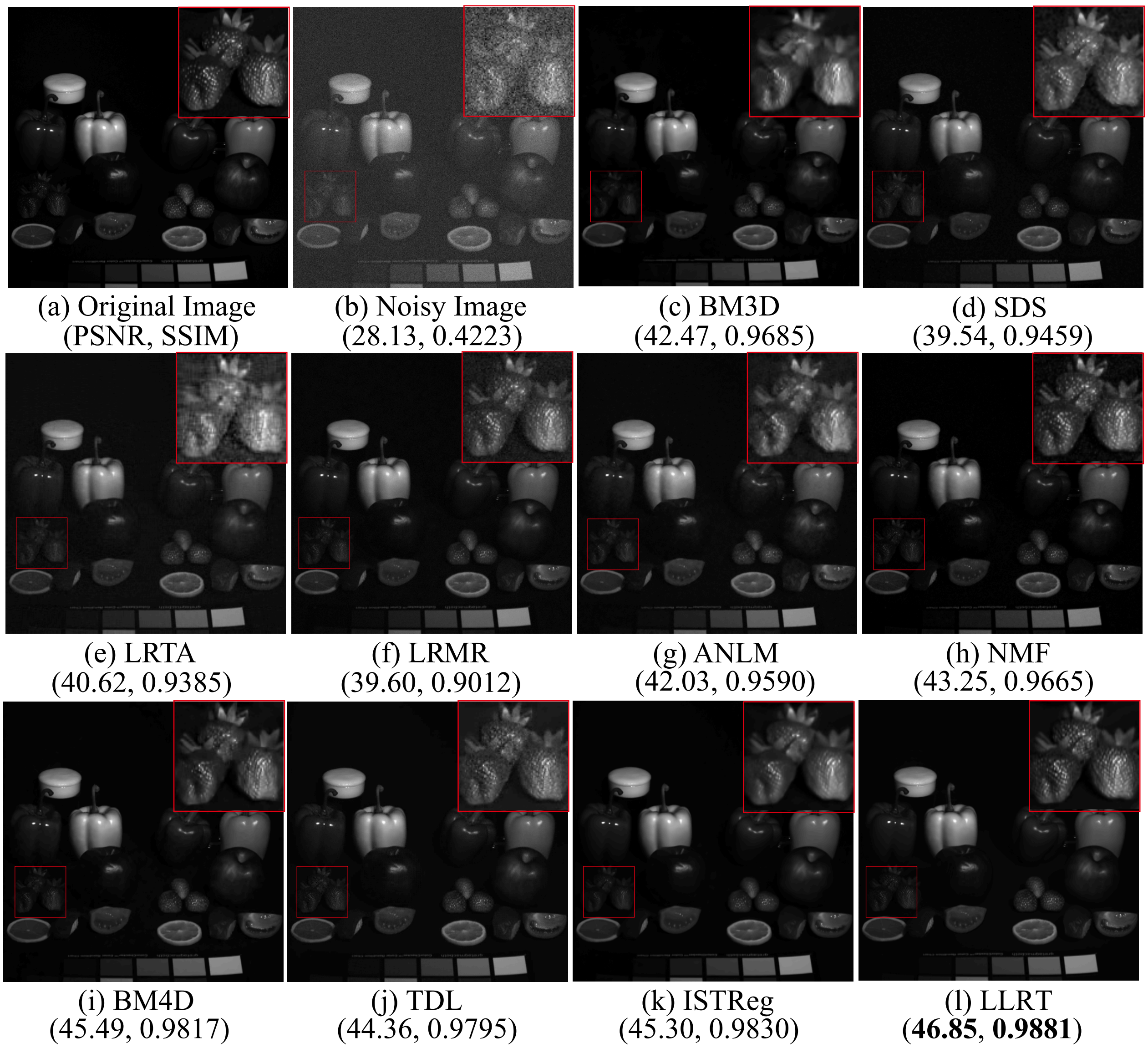

(a) Original Image (PSNR, SSIM) (b) Noisy Image (28.13, 0.4223) (c) BM3D (42.47, 0.9685) (d) SDS (39.54, 0.9459)

(e) LRTA (40.62, 0.9385) (f) LRMR (39.60, 0.9012) (g) ANLM (42.03, 0.9590) (h) NMF (43.25, 0.9665)

(i) BM4D (45.49, 0.9817) (j) TDL (44.36, 0.9795) (k) ISTReg (45.30, 0.9830) (l) LLRT (**46.85**, **0.9881**)

Figure 1. Simulated random noise removal results at 510nm band of image *Food* under noise level λ^2=10 on CAVE dataset.

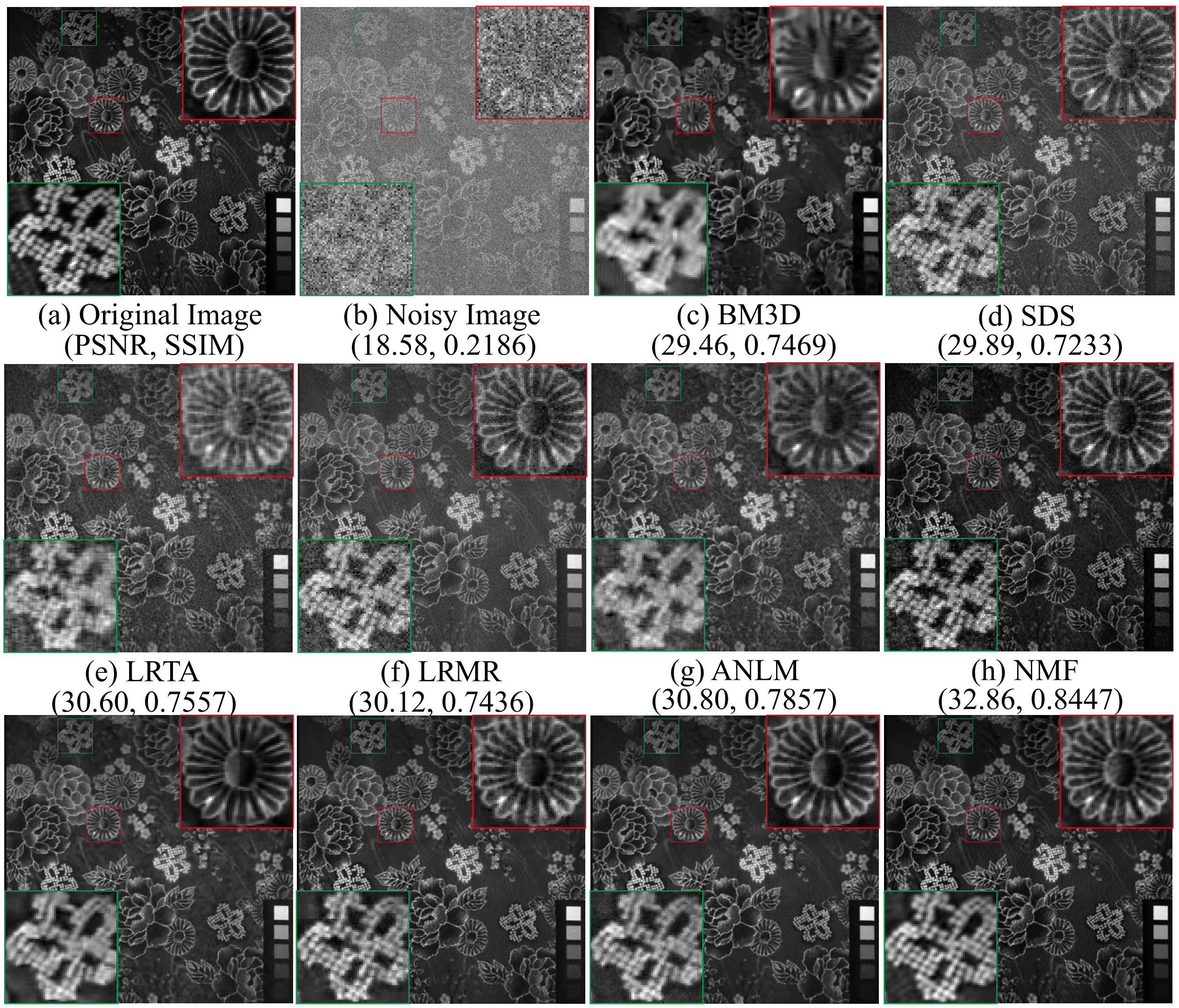

(a) Original Image (PSNR, SSIM)
(b) Noisy Image (18.58, 0.2186)
(c) BM3D (29.46, 0.7469)
(d) SDS (29.89, 0.7233)
(e) LRTA (30.60, 0.7557)
(f) LRMR (30.12, 0.7436)
(g) ANLM (30.80, 0.7857)
(h) NMF (32.86, 0.8447)
(i) BM4D (33.31, 0.8761)
(j) TDL (33.39, 0.8841)
(k) ISTReg (34.06, 0.8887)
(l) LLRT (**35.71**, **0.9221**)

Figure 2. Simulated random noise removal results at 510nm band of image *Cloth* under noise level λ^2=30 on CAVE dataset.

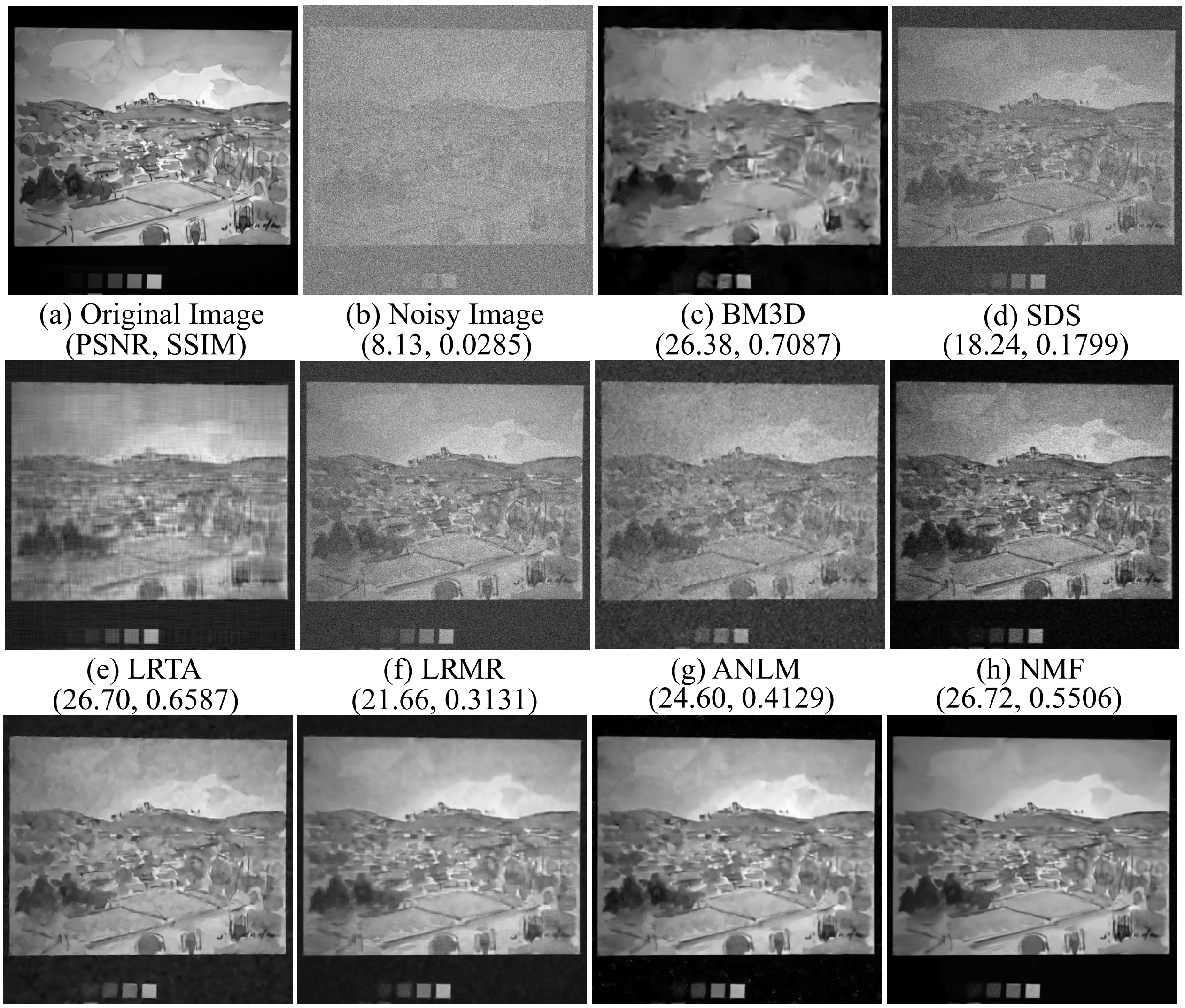

(a) Original Image (PSNR, SSIM)
(b) Noisy Image (8.13, 0.0285)
(c) BM3D (26.38, 0.7087)
(d) SDS (18.24, 0.1799)
(e) LRTA (26.70, 0.6587)
(f) LRMR (21.66, 0.3131)
(g) ANLM (24.60, 0.4129)
(h) NMF (26.72, 0.5506)
(i) BM4D (29.27, 0.7779)
(j) TDL (29.30, 0.8181)
(k) ISTReg (29.76, 0.8540)
(l) LLRT (**31.06**, **0.8813**)

Figure 3. Simulated random noise removal results at 510nm band of image *Watercolor* under noise level λ^2=100 on CAVE dataset.

(a) Original (PSNR:dB) (b) Noisy (22.11) (c) WNNM (29.60)
(d) LSCD (30.57) (e) CBM3D (31.66) (f) LLRT (**31.93**)

Figure 4. Simulated color image *Fox* results under noise level λ^2=20 on BSD dataset.

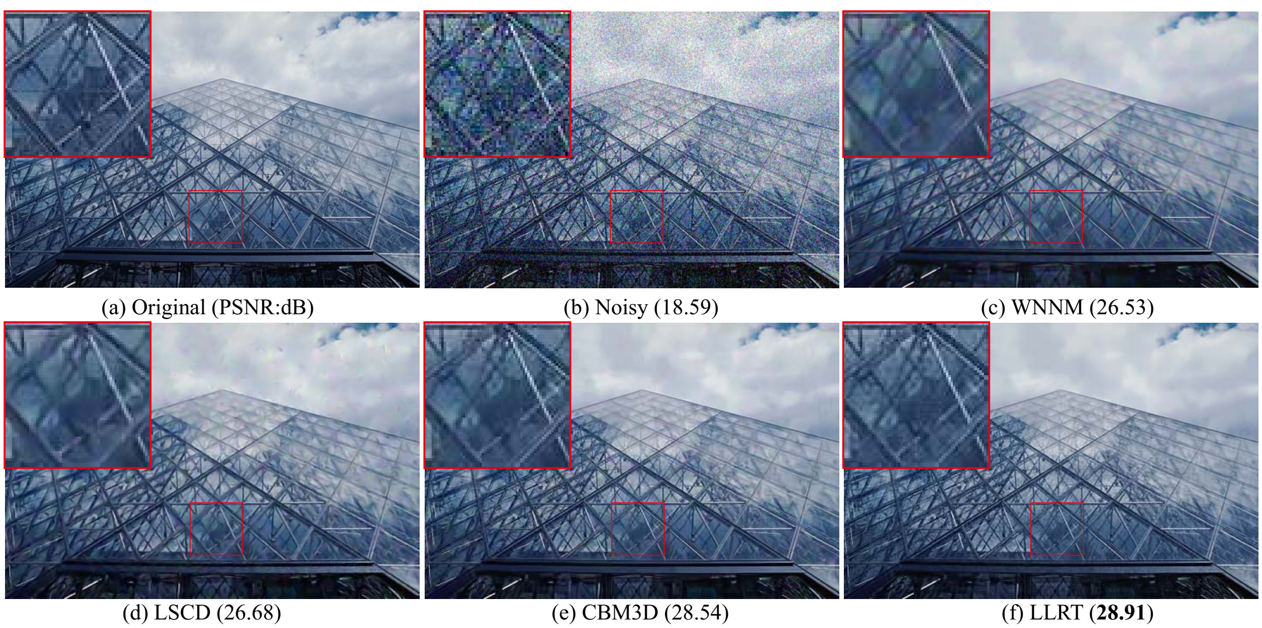

(a) Original (PSNR:dB) (b) Noisy (18.59) (c) WNNM (26.53)
(d) LSCD (26.68) (e) CBM3D (28.54) (f) LLRT (**28.91**)

Figure 5. Simulated color image *Building* results under noise level λ^2=30 on BSD dataset.

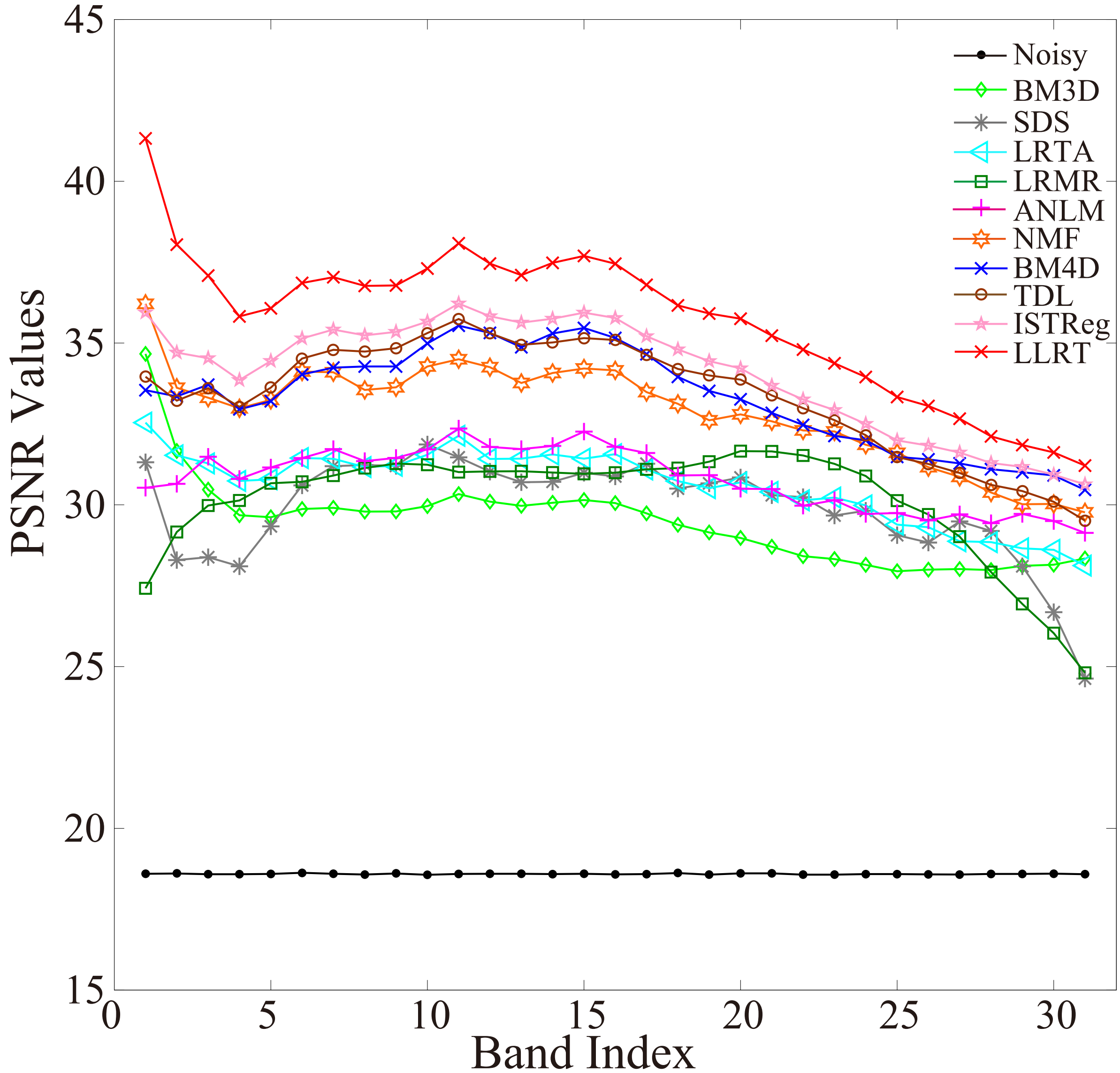

Figure 6. PSNR values of each band of image *Cloth* under noise level λ^2=30 on CAVE dataset.

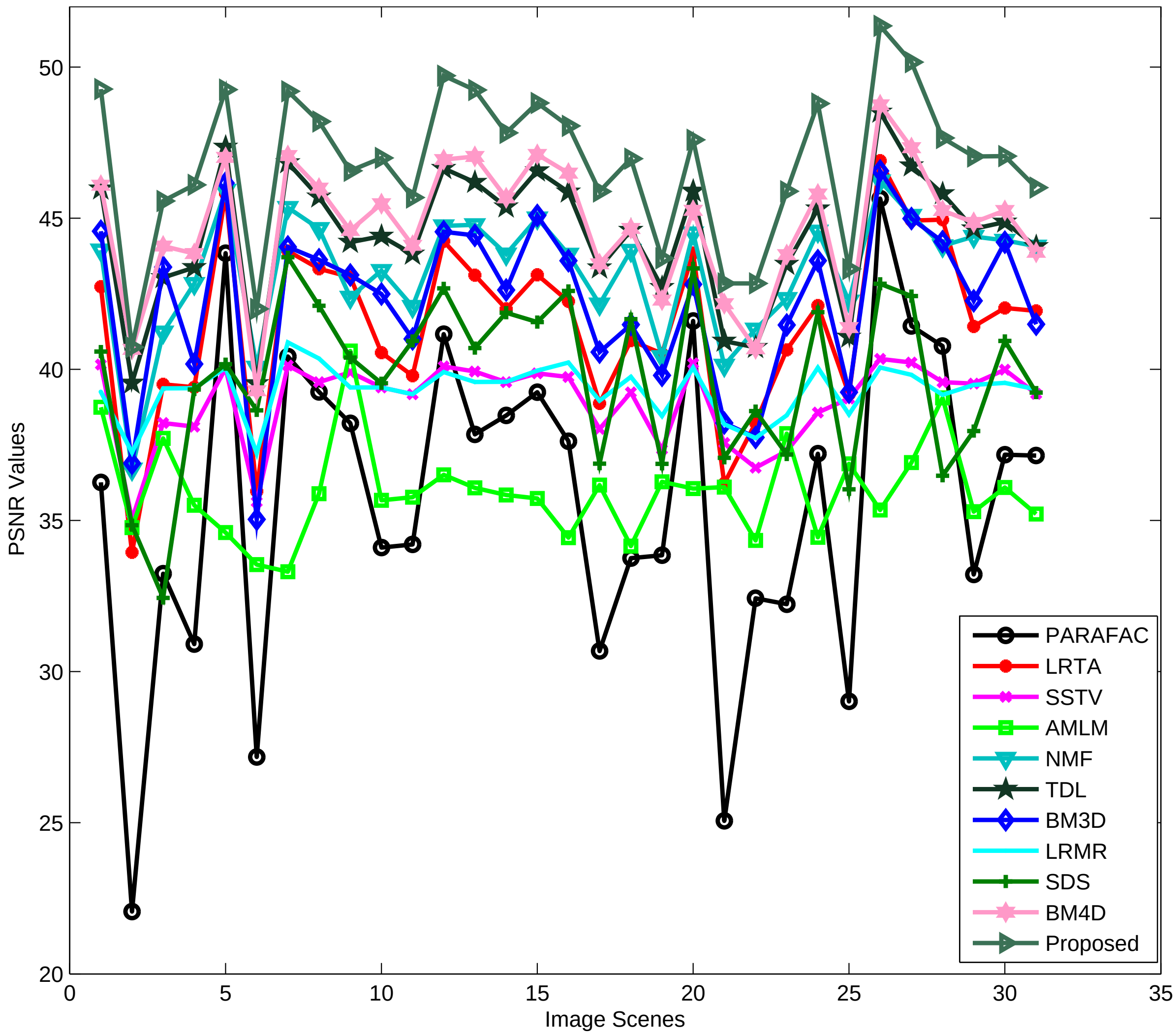

Figure 7. Average PSNR values of all bands of each image under noise level λ^2=30 on CAVE dataset.

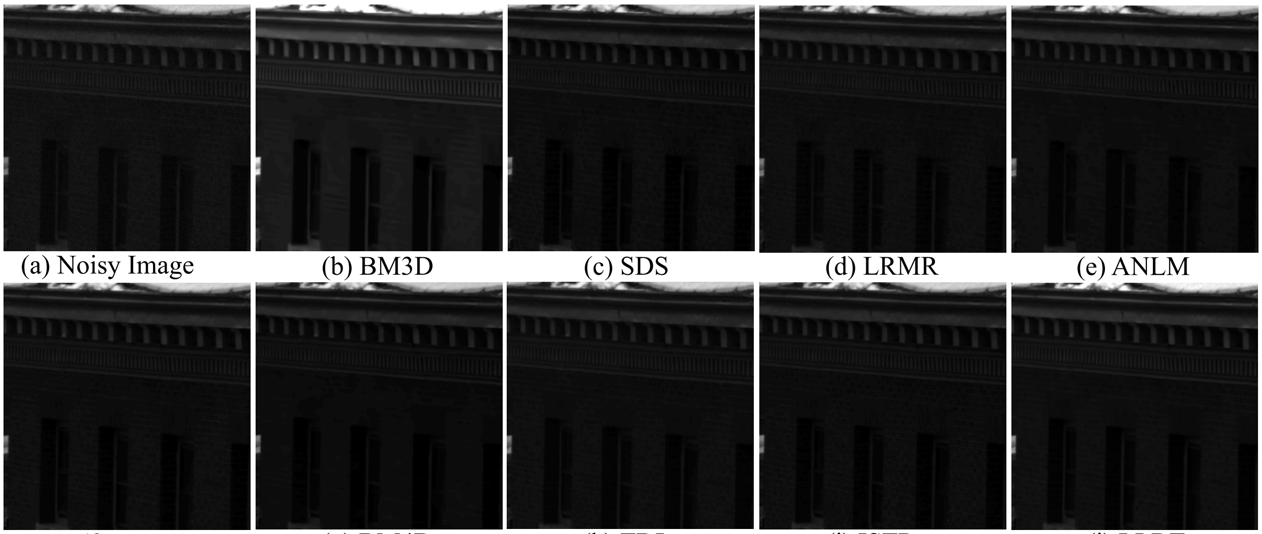

(a) Noisy Image (b) BM3D (c) SDS (d) LRMR (e) ANLM

(f) NMF (g) BM4D (h) TDL (i) ISTReg (j) LLRT

Figure 8. Real random noise removal results at 430nm band of image *Walls* on HHD dataset.

(a) Noisy (b) WNNM (c) LSCD (d) CBM3D (e) LLRT

Figure 9. A real color image noise removal results.

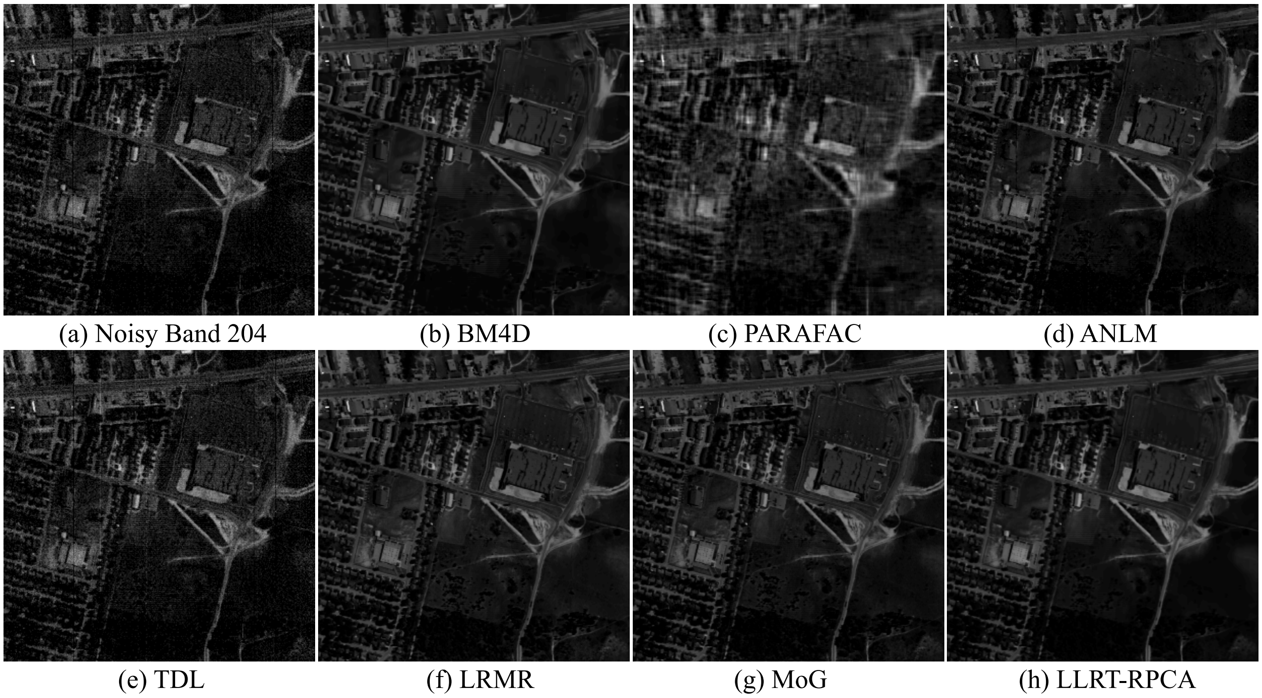

Figure 10. A real HSI mixed noisy removal results.

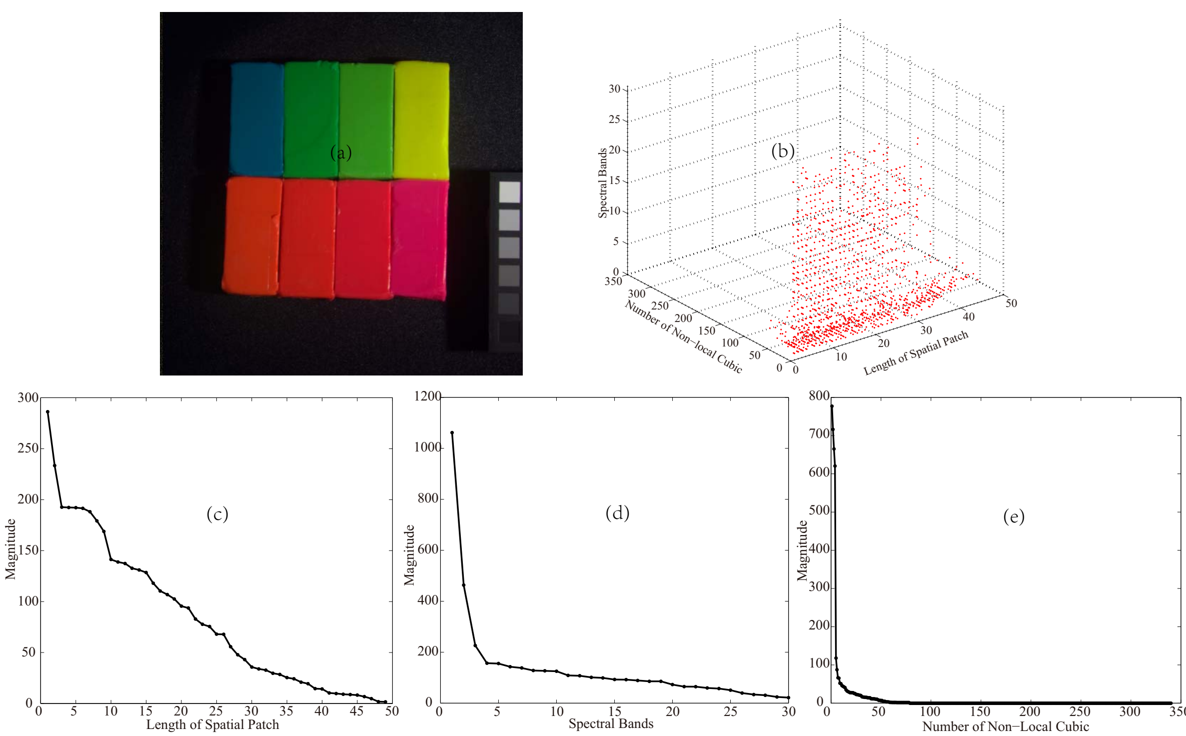

Figure 11. Low-rank property analysis of the constructed 3-order tensor along each mode via HOSVD.

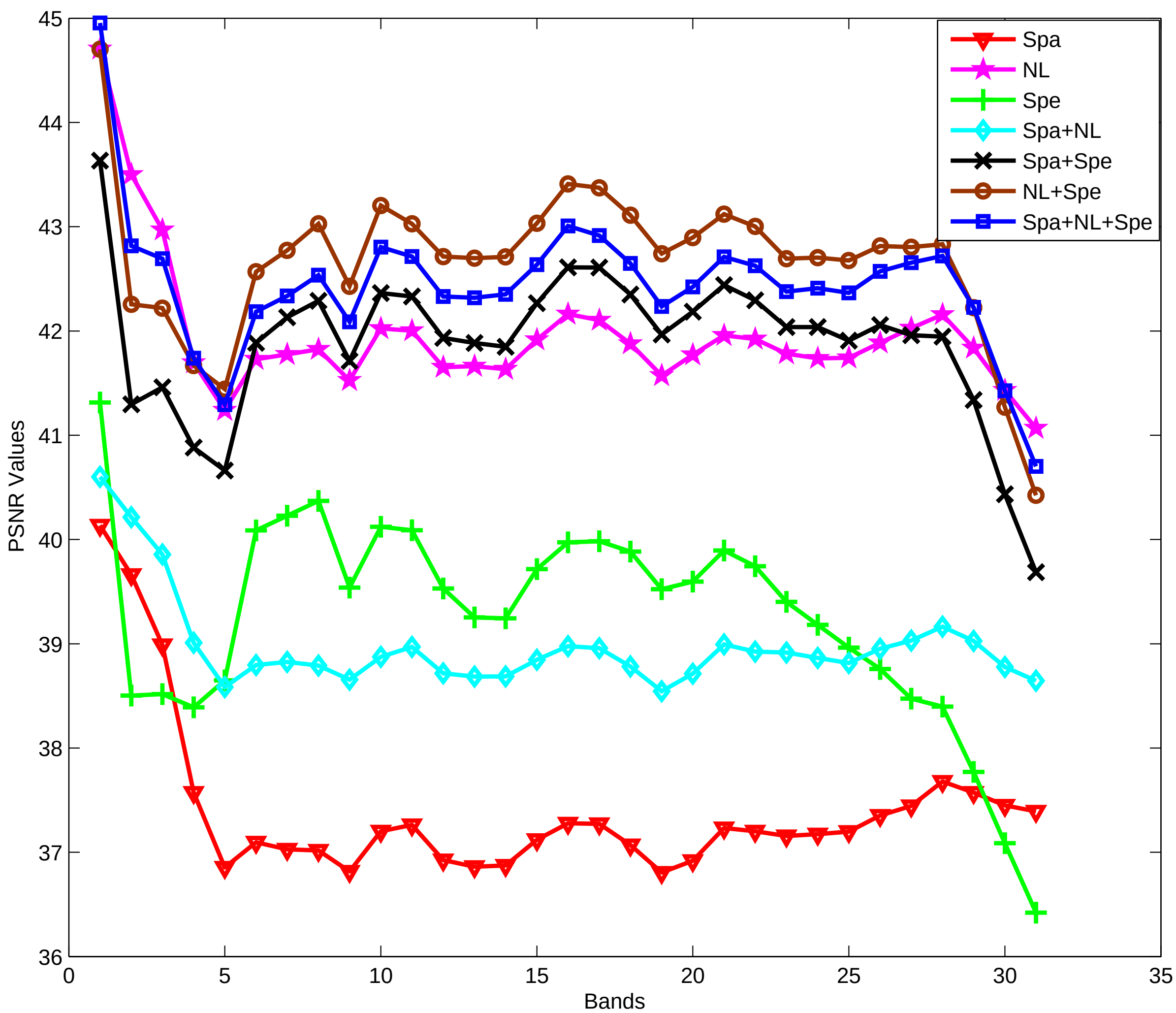

Figure 12. Effectiveness of low-rank prior along each mode and their combination.